PHYSICAL REVIEW APPLIED **19,** 054016 (2023)

Achiral and Chiral Optical Force Within Topological Optical Lattices Generated with Plasmonic Metasurfaces and Tunable Incident Beam

Xi Tang,[1] Yan Kuai,[1] Zetao Fan,[1] Fengya Lu,[1] Haofeng Zang,[1] Junxue Chen,[2] Qiwen Zhan,[3] and Douguo Zhang[1,*]

[1] *Advanced Laser Technology Laboratory of Anhui Province, Department of Optics and Optical Engineering, University of Science and Technology of China, Hefei, Anhui 230026, China*
[2] *College of Science, Guilin University of Technology, Guilin 541004, China*
[3] *School of Optical-Electrical and Computer Engineering, University of Shanghai for Science and Technology, Shanghai 200093, China*

(Received 7 February 2023; revised 28 March 2023; accepted 6 April 2023; published 4 May 2023)

An optical lattice is a platform that is used in studies in multiple branches of physics, e.g., ultracold atoms and microfluidic sorting. Unlike traditional complex optical systems, surface plasmon polaritons enable the generation of optical lattices on a chip. Here, we propose an on-chip scheme to transform five topological optical lattices using tunable polarization and a phase vortex. Using the dipolar approximation and numerical simulations, we demonstrate that the spin density force is the main force for sorting chiral particles in the out-of-plane direction when their radius is more than 100 nm. A microflow system is proposed to trap particles with electric optical lattices and sort chiral particles with spin optical lattices. Our findings offer possible routes toward realization of on-chip optical lattices and enable their potential application in both biology and chemistry, e.g., in simultaneous trapping or excitation of multiple objects and identification and sorting of chiral objects.

DOI: 10.1103/PhysRevApplied.19.054016

I. INTRODUCTION

The optical lattice, which has a periodic field distribution, provides a fundamental platform for study in many branches of physics [1,2]. This type of periodic field is usually generated by interference of multiple plane waves with tunable phase and amplitude profiles [3,4]. Unlike traditional optical lattices, which are mainly used for trapping, the vortex lattice with orbital angular momentum (OAM) has been applied to microfluidic sorting [5] and particle-enhanced diffusion [6]. However, the complexity and the footprint of the overall optical system have limited the development of optical lattices [7]. Fortunately, complex optical systems can be accomplished on specific photonic chips as a result of the development of integrated photonics. Therefore, optical lattices have been realized successfully using semiconductor microcavities [8], atom chips [9], and plasmonic devices [10].

Surface plasmon polaritons (SPPs) exist on the interface between metal films and other environments [11] and provide a perfect platform for the study of light-matter interactions [12,13], with strong local fields and chiral sorting because of their transverse spin angular momentum (SAM) [14,15]. The optical analogy of magnetic quasiparticles, the electric skyrmion lattice, was first generated using a misaligned hexagonal grating structure with SPPs [16]. Additionally, other optical lattices have been proposed, including the meron lattice and the Bloch-skyrmion lattice [17–19]. These lattices can be constructed using symmetry-governed optical lattices [18], photonic crystals in momentum space [20], and optical chiral multilayers [21]. In addition, manipulation of the shape and positioning of the optical skyrmion lattice [22] has been reported. The interactions between these optical lattices and nanoobjects have also been studied for excitation of multiple purely resonant modes [23]. These studies have also developed potential applications of optical quasiparticles in optical traps [24], deep-subwavelength metrology [25], resonant mode manipulation [23], harmonic generation [26], magnetic domains [27], and topological technologies. Recently, the magnetically induced transformation from the square (anti)meron lattice to the hexagonal skyrmion lattice in a chiral magnet has been reported [28]. However, there have been few reports on transformation of multiple topological optical lattices with plasmonic metasurfaces and their interactions with chiral particles.

In this article, we propose an on-chip scheme (a hexagonal structure composed of six sets of plasmonic metasurfaces) for generation of multiple topological optical lattices

---

[*] dgzhang@ustc.edu.cn

© 2023 American Physical Society

by tuning the polarization and OAM of the incident beam. Through the spin-orbit interactions between the incident beam and the plasmonic metasurfaces, the phases of coherent multiple SPPs can be modified and five kinds of optical lattices can be generated. Therefore, our method offers greater flexibility in generating and manipulating optical lattices. Then, using the spin skyrmion lattice as an example, we examine the optical forces exerted on achiral or chiral particles analytically and numerically, and conclude that they are suitable for a sorting method for chiral particles with diameters of more than 100 nm. We also clarify that the main optical force used in sorting comes from the spin density and that its vector direction is controlled by the sign of the OAM. We further discuss the trapping stability and propose a microflow system for trapping and sorting particles. These results for chirality-controlled optical trapping or sorting may suggest a possible route toward optical trapping, identification, and separation of chiral particles. The method also provides potential values for realization of on-chip optical lattices and their corresponding applications with plasmonic metasurfaces.

II. DESIGNED PARAMETERS OF METASURFACES

Using the Jones vector, any polarized beam can be expressed as the superposition of two circularly polarized beams with orbital angular momentum [29],

$$E_{\text{inc}} = \frac{1}{\sqrt{2}} E_{\text{LCP}} \exp(-j\theta + jl\varphi) + \frac{1}{\sqrt{2}} E_{\text{RCP}} \exp(j\theta + jm\varphi), \tag{1}$$

where l and m are the order of OAM of left and right circularly polarized light (LCP and RCP) and φ is the azimuthal angle. $\varphi = 0$ denotes the x direction, and θ is defined as the angle between the polarized orientation and the x direction. Equation (1) describes a linearly polarized beam with a vortex phase, where $l = m$. In this work, we use a type of plasmonic metasurface to separate the SPPs excited by RCP and LCP [30]. As shown in Fig. 1(a), the plasmonic metasurfaces are carved into a gold film with a thickness of 200 nm. The incident beam illuminates the structure normally from the substrate and excites the SPPs from two sets of plasmonic metasurfaces. These SPPs then propagate toward the center of the entire structure in opposite directions, interfere with each other, and form the near field presented on the Au film surface.

Figure 1(b) shows the parameters used in this paper in detail. The basic unit cell comprises a pair of orthogonal nanoslits with a long axis direction of $\pm\pi/4$ relative to the y axis. The distances by which these two nanoslits are separated from each other in a unit cell are d and $D/2$ in the x and y directions, respectively. The parameters of the chiral metasurfaces are given as follows: $W = 50$ nm, $L = 200$ nm, $d = 155$ nm, $P = 11.5$ μm, and $D = 290$ nm. The incident beam wavelength is 640 nm and the wavelength of the SPPs on the gold-air interface is $\lambda_{\text{SPP}} = 620$ nm. The basis vectors for the polarization are LCP and RCP, and thus SPPs excited by RCP or LCP light will propagate to the left or right sides, respectively, of plasmonic metasurfaces with an additional phase difference of 2θ [30]. We define the coupler as an R-type or L-type structure, which would excite SPPs propagating into the center at (0, 0) with RCP or LCP, respectively. Additionally, to enhance the coupling efficiency for conversion of an incident beam into SPPs, three columns of orthogonal nanoslit pairs are used to construct a set of chiral plasmonic structures that are separated by λ_{SPP} from each other. Figure 1(c) shows the distribution of $|Ez|$ as the incident polarization angle varies from 0° to 180°. The additional phase difference is related to the polarized orientation θ, which means that rotation of the polarization can move the fringes. As Fig. 1(c) shows, the intensity of the fringe would remain almost invariant but the fringe would move. This means that any polygonal shape composed of our metasurfaces will excite SPPs of the same amplitude under application of a linearly polarized beam. Therefore, the structure has the potential to realize optical lattices with polygonal shapes in the x-y plane.

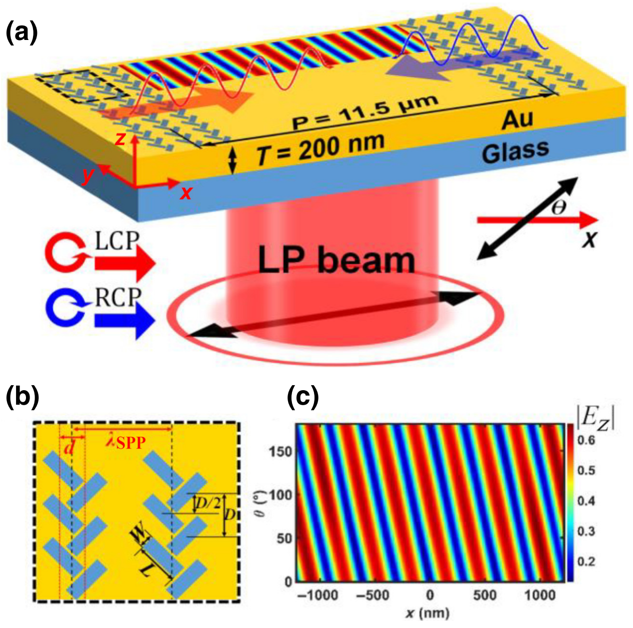

FIG. 1. (a) Schematic of the plasmonic metasurfaces used to separate SPPs excited by the RCP and LCP components of an incident beam. (b) Enlarged fishbone nanoapertures fabricated on a gold film. (c) Simulated demonstration of an extra phase difference controlled by the incident polarization θ.

III. FORMING OPTICAL LATTICES WITH PLASMONIC METASURFACES

To generate optical lattices, we consider polygonal shapes with N sides to excite the propagating SPPs. A parameter σ_n is defined to describe the nth propagating SPP excited by LCP ($\sigma_n = 1$) or RCP ($\sigma_n = -1$) light. Therefore, the electric field can be described using Eq. (2), where ϕ_n is the phase and E_n is the amplitude of the nth SPPs. As we discussed earlier, each side of the plasmonic metasurface can excite SPPs with the same amplitude. In this case, we take $E_n \equiv E_0 = 1$ V/m. The phase ϕ_n consists of the initial phase and the propagating phase. This phase can be expressed using Eq. (3), where $\mathbf{k}_{\rm SPP}$ is the wavevector of SPPs and $\mathbf{r}$ is the position relative to center of hexagonal metasurfaces.

$$E_z(x,y) = \exp(-|k_z|z)\sum_{n=1}^{N} E_n \exp(j\,\phi_n), \tag{2}$$

$$\phi_n = -\sigma_n\theta - \mathbf{k}_{\rm SPP}\cdot\mathbf{r} - (\sigma_n + l)\frac{2\pi n}{N} + \frac{\pi}{2}, \tag{3}$$

$$\mathbf{k}_{\rm SPP}\cdot\mathbf{r} = |k_{\rm SPP}|\left[\cos\left(\frac{2\pi n}{N}\right)x + \sin\left(\frac{2\pi n}{N}\right)y\right]. \tag{4}$$

Using the Maxwell equations, the parallel component in the x-y plane can be written as

$$\begin{pmatrix} E_x(x,y) \\ E_y(x,y) \end{pmatrix} = j\,\frac{|k_z|}{|k_{\rm SPP}|}\sum_{n=1}^{N}\begin{pmatrix} \cos(2\pi n/N) \\ \sin(2\pi n/N) \end{pmatrix} E_{zn}. \tag{5}$$

Therefore, the patterns of the optical lattices can be calculated. We first consider a triangular shape with $N = 3$ that is composed of a pure R-type structure. Figure 2(a) shows the electric field, phase, and spin distributions when the structure is formed using pure R-type plasmonic metasurfaces. The electric field ($|E|$) forms a hexagonally symmetrical lattice and each lattice is composed of a central spot surrounded by six dark spots that correspond to the singularities of the phase distribution. Calculation of the SAM ($\mathbf{L} = \mathrm{Im}(\varepsilon[\mathbf{E}^* \times \mathbf{E}] + \mu[\mathbf{H}^* \times \mathbf{H}])/4\omega$) allows the "up" (red) and "down" (blue) spin vectors in the z direction to be distinguished easily, where $\mathbf{H}$ is the magnetic fields, ω is the frequency, ε and μ are the permittivity and permeability, respectively. The central up and down spin vectors correspond to the singularities of the phase when distributed counterclockwise or clockwise, respectively. If the OAM (l) value of the incident beam changes from -1 to

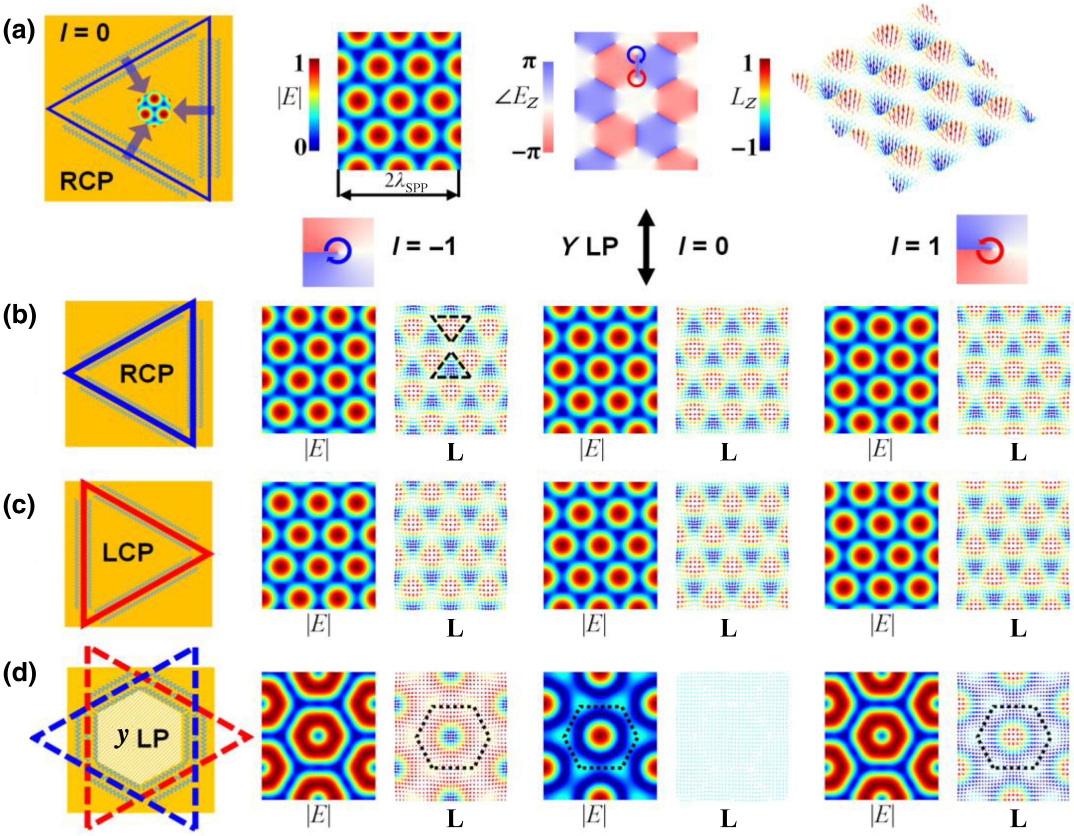

FIG. 2. Schematics of the plasmonic metasurfaces used to generate multiple optical lattices. (a) Distributions of the electric field, phase, and spin of a spin-meron optical lattice generated using a plasmonic metasurface and a RCP beam. Moving optical lattices with tunable incident polarization for the (b) RCP and (c) LCP cases, and the order of the optical vortex phase l. (d) Spin and electric skyrmion lattices generated using plasmonic metasurfaces and a y LP incident beam with different l.

1, the electric field and the spin distribution can also be presented. Figure 2(b) shows that the OAM of the incident beam does not influence the distribution of the optical lattices, except for the position of the lattice center. Additionally, the only difference between the pure L- and R-type structures is that their spin vector directions are opposite to each other [see Fig. 2(c)]. To characterize the topology of the optical lattices, we calculate the topological number Q using [16]

$$Q = \frac{1}{4\pi}\iint_A \mathbf{n}\cdot\left[\left(\frac{\partial \mathbf{n}}{\partial x}\right)\times\left(\frac{\partial \mathbf{n}}{\partial y}\right)\right]dxdy, \tag{6}$$

where A is the area of one unit. $\mathbf{n}$ represents the unit vector in the direction of a three-component physical quantity, such as $\mathbf{E}/|\mathbf{E}|$ or $\mathbf{L}/|\mathbf{L}|$, which correspond to the electric or spin vector directions, respectively. In the triangular region marked in Fig. 2(b), the spin vector varies continuously from the central up or down state to the edge, where the z component of the SAM is zero. The calculated topological number for two Néel-type photonic spin merons is $Q = \pm 1/2$. If a hexagonal shape consists of pure L- or R-type plasmonic metasurfaces, it could form electric skyrmions and spin skyrmions close to each other by tuning the vortex phase to act as a hexagonal grating [24]. The structure is also very robust to polarization because it only couples with LCP or RCP beams.

However, when two groups of triangular shapes with different types of structures are used, we can acquire a hexagonal shape that consists of alternating L- and R-type plasmonic metasurfaces. As illustrated in Fig. 2, we take a linear polarization (y LP) beam carrying different vortex phases as the incident beam. Because any incident beam can be represented using a combination of LCP and RCP, the optical lattice with the misaligned hexagonal shape can be considered as the superposition of the two spin-meron lattices. Optical lattices with spin distributions [i.e., the second and fourth columns of Fig. 2(d)] can be generated when the incident beam carries OAM $l = \pm 1$. The spin distribution remains the same but the vector directions are opposite and are controlled by the sign of the OAM. In the black hexagonal dashed region, the topological number Q corresponding to the spin vector is 1, and thus the optical lattices are spin-skyrmion lattices [18]. For an incident beam without OAM, other optical lattices without spin distributions are acquired. The value of Q is 1 for the electric vector, meaning that this optical lattice is an electric skyrmion lattice [16]. If we rotate the incident polarization from 90° (y LP) to 0° (x LP), another two new optical lattices can then be acquired. Figure 3 depicts the theoretical and simulated results for the distributions of the electric field (E_z) and the phase of the generated optical lattices. In this case, four new optical lattices with a vortex phase (q) in each site are obtained. For the electric vector distribution, they can form an electric skyrmion lattice ($q = 0$) and a honeycomb lattice ($q = 3$) when they are excited together with a tunable polarized beam. For the spin vector distribution, they can form a spin skyrmion lattice ($q = 1$) and a kagome lattice ($q = 2$) with a tunable polarized beam carrying OAM of $l = 1$. The topological numbers are calculated to be 1 for the electric skyrmion ($q = 0$) and the spin skyrmion ($q = 1$), and $\pm 1/2$ for the electric merons ($q = 3$) and the spin merons ($q = 2$). Therefore, it is convenient to realize the transformation of multiple topological optical lattices with plasmonic metasurfaces and a tunable incident beam.

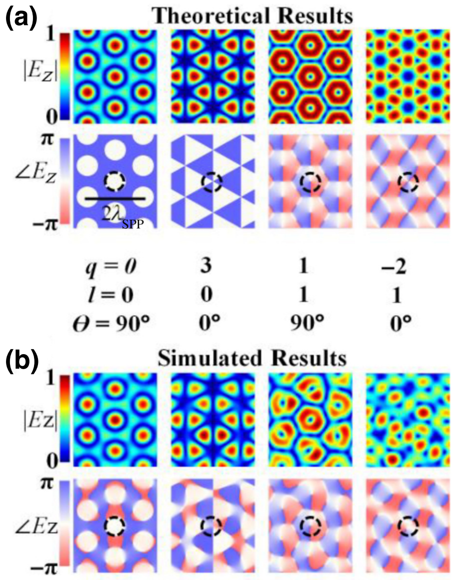

FIG. 3. Electric and phase distributions of multiple optical lattices controlled using the incident polarization and the vortex phase.

IV. PRINCIPLE OF OPTICAL FORCE ON A DIPOLAR PARTICLE IN OPTICAL LATTICES

The electric field and the spin information of topological optical lattices have been presented previously. Other electromagnetic information such as the magnetic field and the time-averaged Poynting vector can be acquired using Maxwell's equations. Therefore, it is possible to calculate the optical force when particles are located within the topological optical lattices.

In general, the optical force acting on a dipolar chiral particle can be expressed as [31]

$$\langle \mathbf{F}\rangle = \frac{1}{2}\mathrm{Re}\left[(\nabla \mathbf{E}^*)\cdot \mathbf{p} + (\nabla \mathbf{H}^*)\cdot \mathbf{m} - \frac{ck_{\mathrm{rm}}^4}{6\pi\sqrt{\varepsilon_{\mathrm{rm}}\mu_{\mathrm{rm}}}}(\mathbf{p}\times\mathbf{m}^*)\right]. \tag{7}$$

Here, **E** and **H** are the electromagnetic fields acting on the particle, c is the speed of light in vacuum, k_{rm} is the wavevector of light in environment, and ε_{rm} and μ_{rm} are the relative electric permittivity and the relative magnetic permeability of the environment, respectively. The induced dipole moments can be written as

$$\begin{bmatrix}\mathbf{p}\\ \mathbf{m}\end{bmatrix}=\begin{bmatrix}\alpha_{\text{ee}} & i\alpha_{\text{em}}\\ -i\alpha_{\text{em}} & \alpha_{\text{mm}}\end{bmatrix}\begin{bmatrix}\mathbf{E}\\ \mathbf{H}\end{bmatrix}, \tag{8}$$

where **p** and **m** are the electric and magnetic moments, respectively, and α_{ee}, α_{mm}, and α_{em} are the electrical polarizability, the magnetic polarizability, and the electromagnetic polarizability of the dipolar particle, respectively.

By putting Eq. (8) into Eq. (7), the expression for the optical force can be obtained as follows:

$$\begin{aligned}\langle\mathbf{F}\rangle = {} & \nabla U+\sigma n_{\text{rm}}\frac{\langle\mathbf{S}\rangle}{c}-\text{Im}[\alpha_{\text{em}}]\nabla\times\langle\mathbf{S}\rangle\\ & -\frac{c\sigma_e}{n_{\text{rm}}}\nabla\times\langle\mathbf{L}_e\rangle-\frac{c\sigma_m}{n_{\text{rm}}}\nabla\times\langle\mathbf{L}_m\rangle+\omega\gamma_e\langle\mathbf{L}_e\rangle\\ & +\omega\gamma_m\langle\mathbf{L}_m\rangle+\frac{ck_{\text{rm}}^4}{12\pi n_{\text{rm}}}\text{Im}[\alpha_{\text{ee}}\alpha_{\text{mm}}^*]\text{Im}[\mathbf{E}\times\mathbf{H}^*],\end{aligned} \tag{9}$$

with the following cross sections:

$$\sigma_e=\frac{k_{\text{rm}}}{\varepsilon_{\text{rm}}\varepsilon_0}\text{Im}[\alpha_{\text{ee}}],\sigma_m=\frac{k_{\text{rm}}}{\mu_{\text{rm}}\mu_0}\text{Im}[\alpha_{\text{mm}}], \tag{10}$$

$$\sigma=\sigma_e+\sigma_m-\frac{c^2k_{\text{rm}}^4}{6\pi\varepsilon_{\text{rm}}}(Re[\alpha_{\text{ee}}\alpha_{\text{mm}}^*]+\alpha_{\text{em}}\alpha_{\text{em}}^*), \tag{11}$$

$$\gamma_e=2\omega\,\text{Im}[\alpha_{\text{em}}]-\frac{ck_{\text{rm}}^4}{3\pi\varepsilon_{\text{rm}}\varepsilon_0 n_{\text{rm}}}\text{Re}[\alpha_{\text{ee}}\alpha_{\text{em}}^*], \tag{12}$$

$$\gamma_m=2\omega\,\text{Im}[\alpha_{\text{em}}]-\frac{ck_{\text{rm}}^4}{3\pi\mu_{\text{rm}}\mu_0 n_{\text{rm}}}\text{Re}[\alpha_{\text{mm}}\alpha_{\text{em}}^*]. \tag{13}$$

where ε_0 and μ_0 are the permittivity and permeability. The first term of Eq. (9) is the gradient force $\mathbf{F}_g$, where $U=1/4(\text{Re}[\alpha_{\text{ee}}]|\mathbf{E}|^2+\text{Re}[\alpha_{\text{mm}}]|\mathbf{H}|^2-2\text{Re}[\alpha_{\text{em}}]\text{Im}[\mathbf{H}\cdot\mathbf{E}^\star])$ is the term that represents the interaction between the particle and the field. The second term is the radiation pressure $\mathbf{F}_r$, which is proportional to the time-averaged Poynting vector $\langle\mathbf{S}\rangle=1/2\text{Re}[\mathbf{E}\times\mathbf{H}^*]$. The third term, which is called the "vortex" force $\mathbf{F}_v$, is determined by the energy flow vortex around the particle and the electromagnetic polarizability. $\langle\mathbf{L}_e\rangle=\varepsilon_{\text{rm}}\varepsilon_0/(4\omega)\text{Im}[\mathbf{E}^*\times\mathbf{E}]$ and $\langle\mathbf{L}_m\rangle=\mu_{\text{rm}}\mu_0/(4\omega)\text{Im}[\mathbf{H}^*\times\mathbf{H}]$ are the time-averaged spin densities. The fourth and fifth terms are both curl-spin forces $\mathbf{F}_{\text{cs}}$ related to the curl of the spin densities; the sixth and seventh terms describe the spin density forces $\mathbf{F}_s$ as they are associated with these spin densities. The final term is related to the alternating flow $\mathbf{F}_f$ of the stored energy.

In our case, the working wavelength is far from the resonance of the chiral particles in the ultraviolet region, and thus the expression for the polarizability can be written as [32]

$$\alpha_{\text{ee}}=4\varepsilon_0\pi r_p^3\frac{(\varepsilon_r-\varepsilon_{\text{rm}})(\mu_r+2)-\kappa^2}{(\varepsilon_r+2\varepsilon_{\text{rm}})(\mu_r+2)-\kappa^2}, \tag{14}$$

$$\alpha_{\text{mm}}=-4\mu_0\pi r_p^3\frac{\kappa^2}{(\varepsilon_r+2\varepsilon_{\text{rm}})(\mu_r+2)-\kappa^2}, \tag{15}$$

$$\alpha_{\text{em}}=-12\pi r_p^3\frac{\kappa\sqrt{\mu_0\varepsilon_0}}{(\varepsilon_r+2\varepsilon_{\text{rm}})(\mu_r+2)-\kappa^2}. \tag{16}$$

where r_p, ε_r, μ_r, and K are the radius, relative permittivity, relative permeability and chiral parameter. The values of $\text{Im}(\alpha_{\text{ee}})$, $\text{Im}(\alpha_{\text{mm}})$, and $\text{Im}(\alpha_{\text{em}})$ are zero, according to Eqs. (14), (15), and (16), respectively. The expression from Eq. (9) can be simplified as follows:

$$\langle\mathbf{F}\rangle=\nabla U+\sigma\frac{\langle\mathbf{S}\rangle}{c}+\omega\gamma_e\langle\mathbf{L}_e\rangle+\omega\gamma_m\langle\mathbf{L}_m\rangle. \tag{17}$$

We now consider a chiral particle with $\varepsilon_r=1.36^2$, $\mu_r=1$, and a chiral parameter κ under the spin skyrmion lattices. Figures 4(a1)–4(a3) present three schematics of the optical forces exerted on a dipolar particle with $\kappa=0$ or ± 1. The particle is placed in the air at a distance of z_0= 300 nm from the interface. If the chiral parameter $\kappa=0$, then the polarizabilities α_{mm} and α_{em} would both be zero, based on Eqs. (15) and (16). Only the gradient force related to the distribution of the electric field $\mathbf{F}_{\text{eg}}$ can be exerted on the particle [Fig. 4(a1)]. The particle will thus be pulled toward the interface, trapped in the circle of the electric field, and form the same optical lattice distribution because of the in-plane optical forces that were reported recently [24]. However, if the chiral parameter κ is not equal to zero, other optical force terms could occur and be exerted on the particle [see Figs. 4(a2) and 4(a3)]. Figure 4(b) shows the electric field, the magnetic field, and the phase and spin distributions of the spin skyrmion lattice excited by the hexagonal metasurfaces and an incident beam with y LP and OAM of $l=-1$. In Fig. 4(c), we present the results of analytical calculations of the total force acting in the z direction at two positions, comprising the center (the center of each unit cell) and the site (the maximum electric field of each unit cell), as the radius of the particles increases. It can obviously be concluded that the optical force exerted on the chiral particles is different when the chiral parameter has the opposite value. To verify this phenomenon more accurately, a full wave simulation is used to calculate the total optical force.

We define the background using Eqs. (2) and (5) directly. The optical force calculations are performed on the outer surface, which encloses the particles, and the results are acquired by integrating the time-averaged

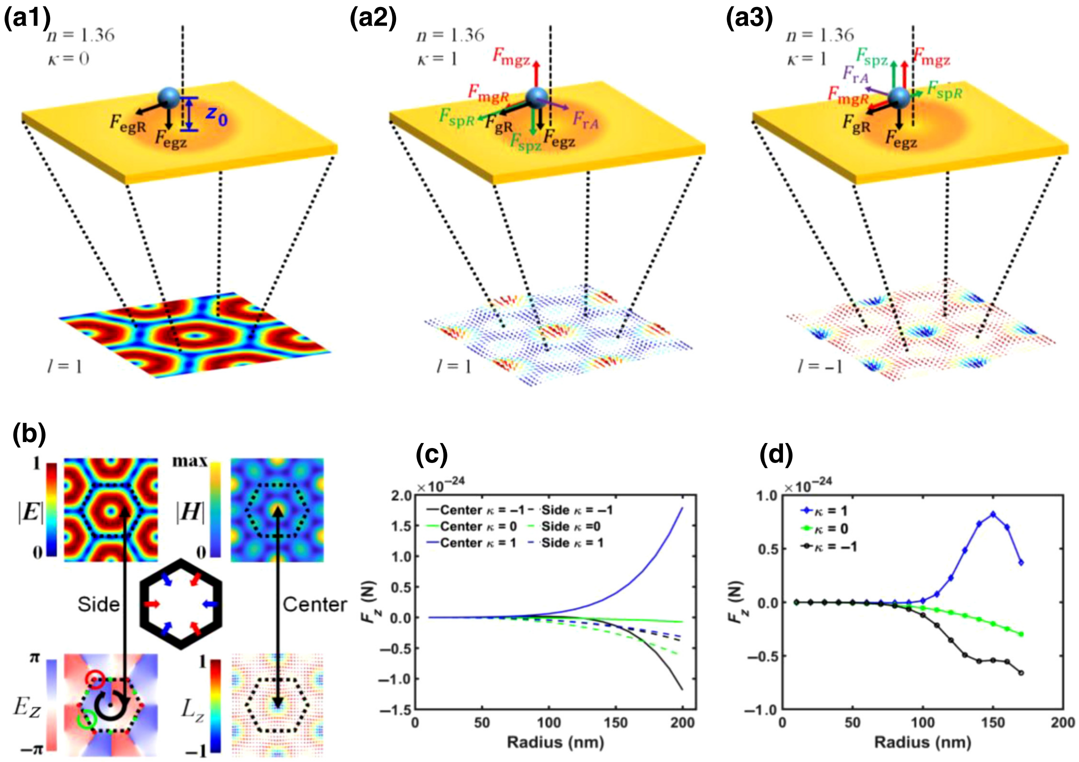

FIG. 4. Schematic view of the directions of all terms of the time-averaged optical forces exerted on the (a1) dielectric or (a2) and (a3) chiral particles when placed over the metal surface. (b) Distribution of the spin skyrmion. (c) Total z component of the optical force calculated using the Rayleigh approximation and comparison of F_z at two different positions in one cell with different values of chiral parameter κ. (d) Total z component of optical force exerted on particles when calculated via a full wave simulation.

Maxwell stress tensor over the closed surface [33]. The tensor and the force are expressed as

$$\langle F_{\text{total}}^{\text{out}}\rangle = \oint \left[\bar{\bar{T}}^{\text{out}}\right]\cdot ds, \tag{18}$$

$$\left\langle\bar{\bar{\mathbf{T}}}\right\rangle = \frac{1}{2}\text{Re}\left[\mathbf{D}_{\text{out}}\mathbf{E}^*_{\text{out}} + \mathbf{B}_{\text{out}}\mathbf{H}^*_{\text{out}} - \frac{1}{2}\bar{\bar{\mathbf{I}}}(\mathbf{E}^*_{\text{out}}\cdot\mathbf{D}_{\text{out}} + \mathbf{H}^*_{\text{out}}\cdot\mathbf{B}_{\text{out}})\right]. \tag{19}$$

Here, "out" means the total external field of the particles and $\bar{\bar{\mathbf{I}}}$ is the unity tensor. The simulated results of the full wave simulation are presented in Fig. 4(d) when the particle is located at the center of a unit cell. We observe phenomena similar to the analytical phenomena. However, when the particle size reaches 150 nm, the force reaches a maximum with $\kappa = 1$. This is because the dipolar approximation is not suitable for use with larger particles, and other poles also contribute to the total forces [33]. Comparison of the analytical and simulated results shows that they agree well with each other and that the chiral particles can be sorted well as the particle size increases.

To enable further discussion of the optical force acting in the z direction, all terms for the optical forces acting along the z axis are presented in Fig. 5. In Fig. 5(a), a chiral particle with $\kappa = 1$ is located at the center of a spin skyrmion. The main contributing terms in this case are the spin density force and the gradient force. In our cases, α_{ee} is positive but α_{mm} is always negative. Because the field decays along the z direction, the electric and magnetic gradient vectors point toward the interface. Then, the gradient forces from the electric field pull the particle toward the interface, while the forces from the magnetic field push the particle away. Because we mainly focus on $\mathbf{F}_z$, Im$[\mathbf{H}\cdot\mathbf{E}^\star]$, and $\langle\mathbf{S}\rangle_z$ being zero, the optical forces related to α_{em} in the z direction come from the spin density only. Figure 5(a) shows that the magnetic gradient force $\mathbf{F}_{\text{mg}}$ is the main optical force when the particle is sufficiently small, while the spin density force $\mathbf{F}_{\text{sp}}$ is dominant for large particles. The electric gradient force $\mathbf{F}_{\text{eg}}$ is quite weak because the amplitude of the electric field is at a minimum at the center of the doughnut shape. When a chiral particle is located at the side of the unit cell, $\mathbf{F}_{\text{eg}}$ becomes the main force, and the particle is then attracted to the interface. However, the value of $\mathbf{F}_{\text{eg}}$ in Fig. 5(b) is still much lower than $\mathbf{F}_{\text{sp}}$ in Fig. 5(a) when the radius exceeds 150 nm. Figure 5(c) presents the optical forces exerted on particles with $\kappa = -1$. In this case, $\mathbf{F}_{\text{mg}}$ is the same as that shown in Fig. 5(a), while $\mathbf{F}_{\text{sp}}$ is opposite to the previous case.

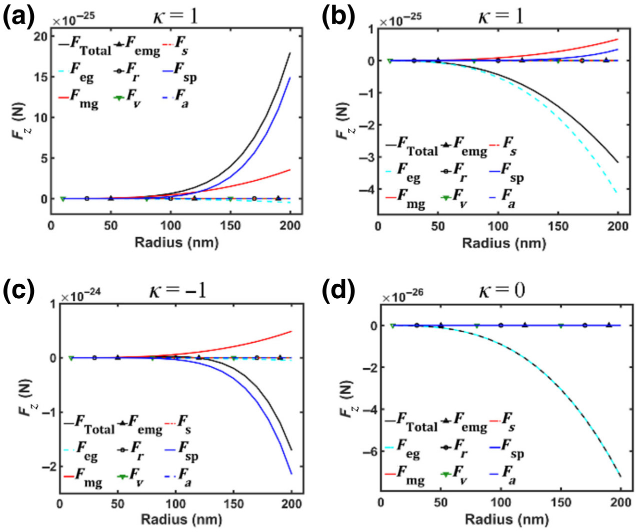

FIG. 5. Contributions of the z component of the optical forces exerted on the chiral particle under an incident beam with $\theta = 90^\circ$ and $l = -1$. The chiral particle with $\kappa = 1$ is located at the center (a) and the side (b) of one cell, as defined in Fig. 4(b). The chiral particle with (c) $\kappa = -1$ or (d) 0 is located at the center of one cell.

This means that the spin skyrmion lattice can be used to trap chiral particles with $\kappa = -1$ and to push away chiral particles with $\kappa = 1$. This shows the potential for use of this approach to sort chiral particles in the z direction. For comparison, the optical forces that are exerted on achiral particles are plotted in Fig. 5(d). Only the electric gradient force can be observed in this case.

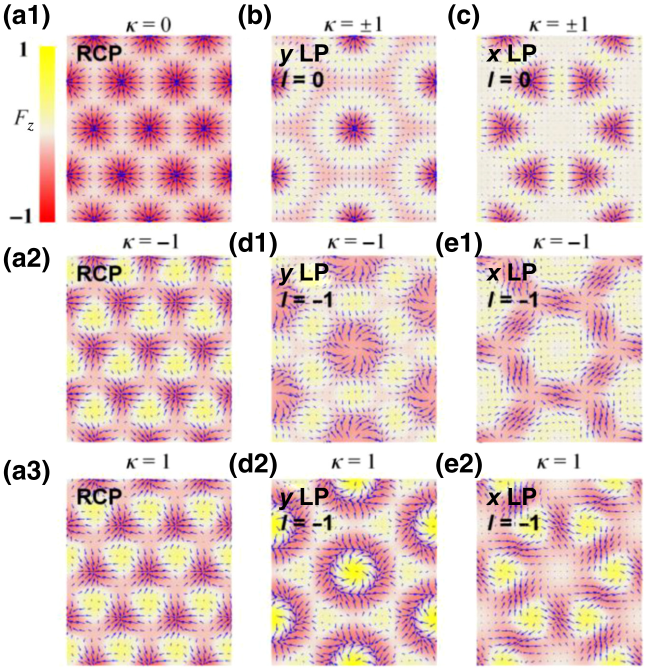

FIG. 6. Optical forces exerted by plasmonic lattices with plasmonic metasurfaces. The in-plane force vector directions (arrows) and magnitudes (arrow sizes) are shown in the generated optical lattices, with the background color representing the distribution of the out-of-plane force F_z. Particles with different values of the chiral parameter κ are trapped by (a1)–(a3) a spin-meron lattice, (b) an electric skyrmion lattice, and (c) a honeycomb lattice. The chiral particles with the opposite chiral parameter κ are sorted into (d1),(d2) a spin skyrmion lattice and (e1),(e2) a kagome skyrmion lattice. The results in all panels are calculated using Eqs. (2), (5), and (17) with the tunable incident polarization and vortex phase.

Figure 6 shows the distributions of the total optical forces on a 150-nm particle in the x-y plane. The arrows represent the vector directions and amplitudes of the in-plane optical forces. The background is the z component of the normalized optical force $F_z/|F|_{\max}$. Figures 6(a1)–6(a3) show the optical forces in the spin-meron lattice when the incident beam is RCP. Regardless of the chiral parameter, the particles can be trapped in this case. However, the chiral particles may not be stable because the F_z is smaller than that for the achiral particle case. For the other four topological optical lattices, the forces exerted on achiral particles have been discussed in recent research [24]. The particles will form the same lattices as the optical lattices used for trapping. In Figs. 6(b) and 6(c), only the electric and magnetic gradient forces can be induced by electric optical lattices, and thus the chiral particles cannot be sorted. In Figs. 6(d1) and 6(d2), the forces exerted on the chiral particles with different κ values are very different in a spin-skyrmion lattice. A particle with $\kappa = -1$ would be pulled downward, while a particle with $\kappa = 1$ would be pushed away. This phenomenon can be observed in Figs. 6(e1) and 6(e2). All results presented here indicate the possibility of trapping and sorting chiral particles using our plasmonic metasurfaces through tuning of the incident polarization and the vortex phase.

V. A MICROFLOW SYSTEM FOR SORTING PARTICLES

In this section, we further discuss the trapping stability and analyze the behavior of particles with different chirality in optical lattices. To clearly show the sorting and trapping of particles, we set the incident power to 20 mW and assume the density of a dielectric particle ($n = 1.36$) with radius 150 nm is $\rho = 1.05 \times 10^3$ kg m^{-3}. Then, the mass and gravity of the particle are 1.48×10^{-17} kg and 1.45×10^{-4} pN. The annular incident beam [34] is adopted to ensure the same excitation efficiency of SPPs from incident beam with or without vortex phase. The area of illumination region is $S_0 = \pi[(P/2 + \lambda_{\mathrm{SPP}})^2 - (P/2 - \lambda_{\mathrm{SPP}})^2] \approx 4.48 \times 10^{-11}$ m^2, where P is the distance between the center of two sets of chiral metasurface shown in Fig. 1(a). If we do not consider the field enhancement of SPPs and assume the electric amplitude E_n is equal to incident electric amplitude, all optical forces shown previously just need to be multiplied by a scale factor $f_s = |E_{\text{inc}}|^2/|E_0|^2 = 2c\mu_0 P_{\text{inc}}/S_0/|E_0|^2 \approx 3.36 \times 10^{11}$. For example, the out-of-plane force (F_z) on a 150-nm chiral particle shown in Fig. 5(a) would be 0.133 pN.

The trapping potential is used to determine the stability of the optical tweezer, which can be calculated by the formula [35]

$$U(r_1) = \int_{r_0}^{r_1} \mathbf{F}(r) d\mathbf{r}. \tag{20}$$

To trap particles stably, the trapping potential must be deep enough to overcome the kinetic energy of the particle in Brownian motion, $k_B T$, where k_B is the Boltzmann constant and T is the absolute temperature of the environment. Here, we set T as 300 K. Figure 7(a) shows the distribution of the transverse trapping potential (U_{xy}) generated by the in-plane force (F_x, F_y) and the out-of-plane force (F_z) on a particle with $\kappa = 0$ placed in an electric skyrmion lattice. The potential of "side" in Fig. 4(b) is chosen as the zero of the potential energy. The distance between this particle and the surface of the gold film is $z_0 = 300$ nm. The potential depth is larger than 1 $k_B T$, which means the particle can be stably trapped in the center of a lattice unit. Meanwhile, the particle would be pulled towards the interface because $F_z < 0$. Figures 7(b) and 7(c) present the cross sections of U_{xy} and F_z on different chiral particles along $x = 0$. The potential depth of chiral particles is lower than that of achiral particles but still larger than 1 $k_B T$, so all particles can be trapped in the x-y plane and form the same distribution as the optical lattice. The corresponding potential field (U_{xy}) and out-of-plane force (F_z) for transforming the electric skrymion lattice to a spin skyrmion lattice are shown in Figs. 7(d) and 7(e). The potential of "center" in Fig. 4(b) is chosen as the zero of the potential energy. Particles can be trapped in the ring valley shown in Fig. 7(d). Then, chiral particles can move in this ring due to the azimuthally in-plane force (nonconservative force) shown in Figs. 6(d1) and 6(d2). Additionally, achiral particles and chiral particles with $\kappa = -1$ can be pulled towards the interface while chiral particles with $\kappa = 1$ are pushed away because $F_z > 0$ around the potential valley.

Based on these conclusions, we propose a microflow system for trapping and sorting particles. In Fig. 8(a), mixed particles with different chirality are injected into the microflow cavity from port A. The chiral particles with $\kappa = 1$ are pushed away from interface and other particles are pulled down to the interface in the spin skyrmion lattice. Then, the main components of the mixed particles from port B are the chiral particles with $\kappa = 1$. In order to discuss the motion of a particle in an optical lattice, the equation of motion can be written as

$$G(z) + F_b(z) + F_{\text{Brown}}(\mathbf{r}, t) - \gamma \left(\frac{dr}{dt} - v_f \right) + F_{\text{trap}}(\mathbf{r}) = m \frac{d^2\mathbf{r}}{dt^2}, \tag{21}$$

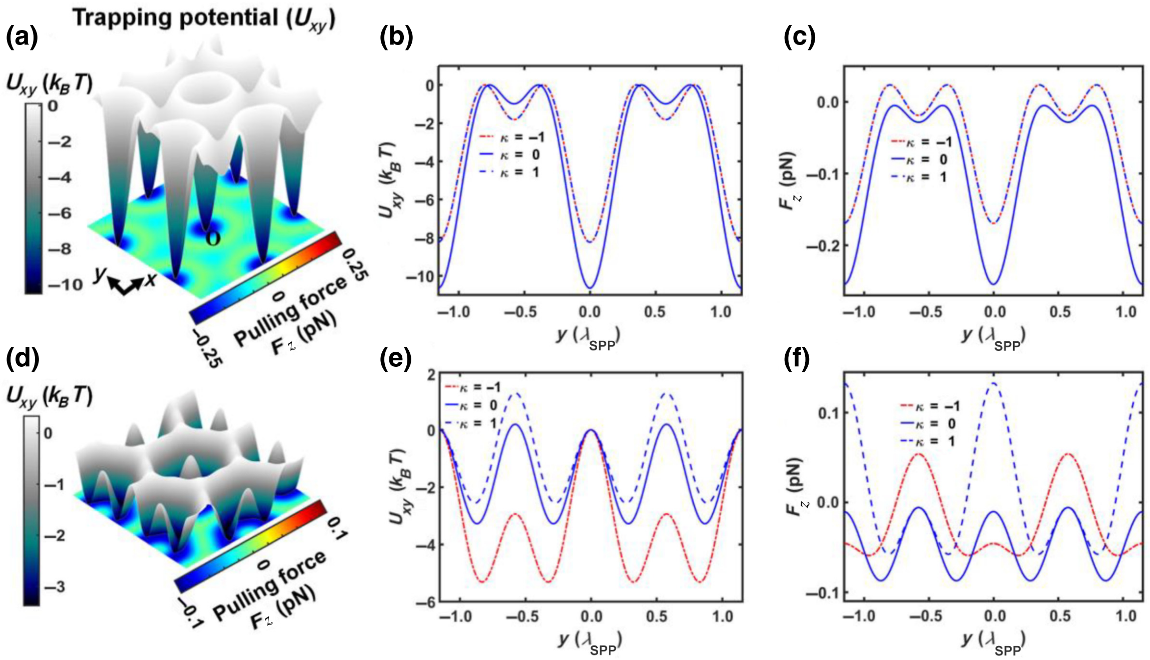

FIG. 7. (a) The transverse trapping potential (U_{xy}) produced by in-plane force (F_x, F_y) and the out-of-plane force (F_z) on an achiral particle placed in an electric skyrmion lattice. (b),(c) Cross sections of U_{xy} and F_z on different chiral particles along $x = 0$. The difference between (a)–(c) and (d)–(f) is that the electric skyrmion lattice is replaced by a spin skyrmion lattice. The power of the annular incident beam is 20 mW.

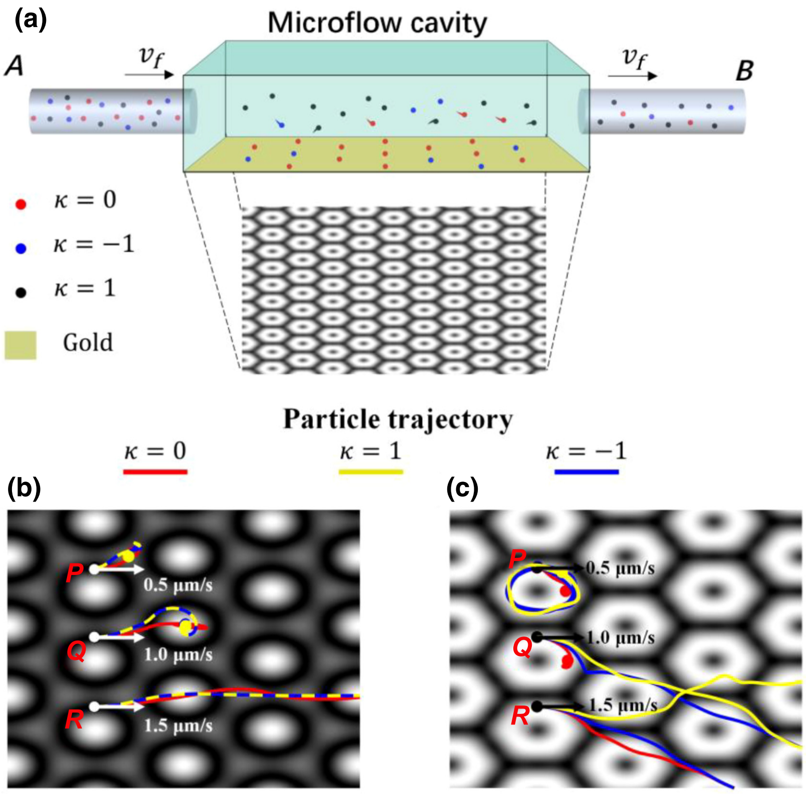

FIG. 8. (a) Schematic of the setup for trapping and sorting particles. v_f is the velocity of the fluid. (b),(c) A 5 s trajectory of a dielectric particle in an electric skyrmion lattice and a spin skyrmion lattice without considering out-of-plane force (F_z). Three points (P, Q, and R) are the initial positions when v_f changes from 0.5 μm s^{-1} to 1.5 μm s^{-1}.

where G is gravity, F_b is buoyancy, $F_{\text{Brown}}(\mathbf{r}, t)$ represents the Brownian motion, γ is the friction coefficient ($\gamma = 6\pi r_p \eta$, with η being the viscosity; for air at $T = 293.15$ K, $\eta = 1.83 \times 10^{-5}$ kg m^{-1} s^{-1}, v_f is the velocity of the fluid and $F_{\text{trap}}(\mathbf{r})$ is the external optical force from optical lattices. For simplicity, we ignore the Brownian motion and just analyze the motion of particles in the x-y plane. Equation (21) can be simplified as

$$-\gamma\left(\frac{dr}{dt} - v_f\right) + F_{\text{trap}}(\mathbf{r}) = m\frac{d^2\mathbf{r}}{dt^2}. \tag{22}$$

Then, we calculate the particle trajectory using the finite-difference method. We place a particle at the side defined in Fig. 4(b) and assume the initial velocity of this particle is the same as that of the fluid. The interval of time is chosen as 0.5 ms and the total recording time is 5 s. Figure 8(b) shows the motion of chiral particles in an electric skyrmion lattice. P, Q, and R correspond to three cases in which the velocity of the fluid is different. Particles can be trapped at the corner of a lattice unit with $v_f = 0.5$ μm s^{-1}. If the velocity of fluid increases to 1 μm s^{-1}, particles can be trapped at the center of another lattice unit. When the velocity of the fluid increases to 1.5 μm s^{-1}, the electric optical lattice cannot trap the particles in the x-y plane. The same process can be found in Fig. 8(c) for the spin skyrmion lattice. As we discussed previously, the achiral particle is trapped in the ring and the chiral particles move in the ring when the velocity of the fluid is 0.5 μm s^{-1}. The gradient force of the chiral particles cannot provide enough centripetal force if the velocity of the fluid is 1 μm s^{-1}. Then, the chiral particles cannot move in the ring and escape from the lattice unit. When $v_f = 1.5$ μm s^{-1}, the optical lattice cannot trap all particles, either. From these results, our setup can trap and sort particles through switching two kinds of optical lattice. Firstly, an electric skyrmion lattice is used to trap all particles at the center of each lattice unit. Secondly, the electric skyrmion lattice is transformed to a spin skyrmion lattice using an incident beam with vortex phase order $l = -1$. The particles with $\kappa = 1$ would be pushed away while other particles can be trapped in the ring of each unit. Thirdly, the particles with $\kappa = -1$ can also be pushed away from interface when the order of the vortex phase is changed from -1 to 1. Finally, if we keep increasing the velocity of the fluid, the achiral particles trapped in the gold film can be carried to port B and collected.

VI. CONCLUSION

In summary, we explore the spin and orbital interactions between incident beams and plasmonic metasurfaces theoretically and numerically. By changing the incident polarization and adding a vortex phase, five kinds of optical lattice are easily generated with the plasmonic metasurfaces, including triangular Abrikosov lattices, an electric-type optical skyrmion lattice ($q = 0$), a spin-type optical skyrmion lattice ($q = 1$), a kagome lattice ($q = 2$), and a honeycomb lattice ($q = 3$). Our method provides more routes for manipulation of optical lattices on a chip. In addition, the optical lattices with or without spin distributions could be applied to trapping or sorting chiral particles. We show analytically and numerically that these optical lattices can induce not only gradient optical forces but also spin density forces on dipolar chiral particles with different chirality to realize effective sorting of chiral particles in the z direction. The results of this chirality-controlled optical trapping and manipulation may provide a possible route toward the optical identification and separation of chiral particles. This structure also avoids the use of multiple surface structures or complex optical systems such as multiple beams with different phases [22]. In addition, the ability to switch between multiple lattices has potential for applications in biology, chemistry, and physics, including simultaneous trapping, rotation, and sorting of multiple particles and quasiparticles [36,37], manipulation of light emission, selective excitation of quantum emitters organized in multiple arrays [38], or exploration of new light-matter interactions [39,40] such as interaction with an electron wave packet [41]. We believe that this work offers alternative possibilities for manipulation of on-chip optical lattices and their corresponding applications.

ACKNOWLEDGMENTS

This work was supported in part by the National Natural Science Foundation of China under Grants No. 12134013 and No. 62127818, in part by the National Key Research and Development Program of China under Grant No. 2021YFA1400700, in part by the Fundamental Research Funds for the Central Universities under Grant No. WK2340000109, in part by the Key Research & Development Program of Anhui Province under Grant No. 202104a05020010, and in part by the Hefei Municipal Natural Science Foundation under Grant No. 2021007.

[1] I. Bloch, J. Dalibard, and W. Zwerger, Many-body physics with ultracold gases, Rev. Mod. Phys. **80**, 885 (2008).

[2] X. Luo, L. Wu, J. Chen, R. Lu, R. Wang, and L. You, Generating an effective magnetic lattice for ultracold atoms, New J. Phys. **17**, 083048 (2015).

[3] M. Padgett and R. Bowman, Tweezers with a twist, Nat. Photonics **5**, 343 (2011).

[4] S. Safaei, C. Miniatura, and B. Grémaud, Triangular and honeycomb lattices of cold atoms in optical cavities, Phys. Rev. A **92**, 043810 (2015).

[5] M. P. MacDonald, G. C. Spalding, and K. Dholakia, Microfluidic sorting in an optical lattice, Nature **426**, 421 (2003).

[6] S. Albaladejo, M. I. Marqués, F. Scheffold, and J. J. Sáenz, Giant enhanced diffusion of gold nanoparticles in optical vortex fields, Nano Lett. **9**, 3527 (2009).

[7] T. C. Liew, Y. G. Rubo, and A. V. Kavokin, Generation and Dynamics of Vortex Lattices in Coherent Exciton-Polariton Fields, Phys. Rev. Lett. **101**, 187401 (2008).

[8] J. Scheuer and M. Orenstein, Optical vortices crystals: Spontaneous generation in nonlinear semiconductor microcavities, Science **285**, 230 (1999).

[9] C. J. E. Straatsma, M. K. Ivory, J. Duggan, J. Ramirez-Serrano, D. Z. Anderson, and E. A. Salim, On-chip optical lattice for cold atom experiments, Opt. Lett. **40**, 3368 (2015).

[10] Z. Liu, Y. Wang, J. Yao, H. Lee, W. Srituravanich, and X. Zhang, On-chip optical lattice for cold atom experiments, Nano Lett. **9**, 462 (2009).

[11] W. L. Barnes, A. Dereux, and T. W. Ebbesen, Surface plasmon subwavelength optics, Nature **424**, 824 (2003).

[12] W.-Y. Tsai, J.-S. Huang, and C.-B. Huang, Selective trapping or rotation of isotropic dielectric microparticles by optical near field in a plasmonic Archimedes spiral, Nano Lett. **14**, 547 (2014).

[13] M. Ghorbanzadeh and S. Darbari, Efficient plasmonic 2D arrangement and manipulation system, suitable for controlling particle–particle interactions, J. Lightwave Technol. **37**, 2058 (2019).

[14] M. H. Alizadeh and B. M. Reinhard, Transverse chiral optical forces by chiral surface plasmon polaritons, ACS Photonics **2**, 1780 (2015).

[15] K. Y. Bliokh, A. Y. Bekshaev, and F. Nori, Extraordinary momentum and spin in evanescent waves, Nat. Commun. **5**, 3300 (2014).

[16] S. Tsesses, E. Ostrovsky, K. Cohen, B. Gjonaj, N. H. Lindner, and G. Bartal, Optical skyrmion lattice in evanescent electromagnetic fields, Science **361**, 993 (2018).

[17] A. Ghosh, S. Yang, Y. Dai, Z. Zhou, T. Wang, C.-B. Huang, and H. Petek, A topological lattice of plasmonic merons, Appl. Phys. Rev. **8**, 041413 (2021).

[18] X. Lei, A. Yang, P. Shi, Z. Xie, L. Du, A. V. Zayats, and X. Yuan, A Topological Lattice of Plasmonic Merons, Phys. Rev. Lett. **127**, 237403 (2021).

[19] Q. Zhang, Z. Xie, P. Shi, H. Yang, H. He, L. Du, and X. Yuan, Optical topological lattices of Bloch-type skyrmion and meron topologies, Photonics Res. **10**, 947 (2022).

[20] C. Guo, M. Xiao, Y. Guo, L. Yuan, and S. Fan, Meron Spin Textures in Momentum Space, Phys. Rev. Lett. **124**, 106103 (2020).

[21] Q. Zhang, Z. Xie, L. Du, P. Shi, and X. Yuan, Bloch-type photonic skyrmions in optical chiral multilayers, Phys. Rev. Res. **3**, 023109 (2021).

[22] C. Bai, J. Chen, Y. Zhang, D. Zhang, and Q. Zhan, Dynamic tailoring of an optical skyrmion lattice in surface plasmon polaritons, Opt. Express **28**, 10320 (2020).

[23] Q. Zhang, Z. Liu, F. Qin, S. J. Zeng, D. Zhang, Z. Gu, X. Liu, and J. J. Xiao, Exploring optical resonances of nanoparticles excited by optical skyrmion lattices, Opt. Express **27**, 7009 (2019).

[24] S. Tsesses, K. Cohen, E. Ostrovsky, B. Gjonaj, and G. Bartal, Spin-orbit interaction of light in plasmonic lattices, Nano Lett. **19**, 4010 (2019).

[25] L. Du, A. Yang, A. V. Zayats, and X. Yuan, Deep-subwavelength features of photonic skyrmions in a confined electromagnetic field with orbital angular momentum, Nat. Phys. **15**, 650 (2019).

[26] J. Watzel and J. Berakdar, Topological light fields for highly non-linear charge quantum dynamics and high harmonic generation, Opt. Express **28**, 19469 (2020).

[27] X. Lei, L. Du, X. Yuan, and A. V. Zayats, Topological light fields for highly non-linear charge quantum dynamics and high harmonic generation, Nanophotonics **10**, 3667 (2021).

[28] X. Z. Yu, W. Koshibae, Y. Tokunaga, K. Shibata, Y. Taguchi, N. Nagaosa, and Y. Tokura, Transformation between meron and skyrmion topological spin textures in a chiral magnet, Nature **564**, 95 (2018).

[29] Y. Cai, W. Liu, W. Yang, J. Xu, H. Yang, and K. Shi, Differential fluorescence microscopy by using a dynamic cylindrical-vector field, Opt. Lett. **46**, 2332 (2021).

[30] Q. Tan, Z. Xu, D. H. Zhang, T. Yu, S. Zhang, and Y. Luo, Polarization-controlled plasmonic structured illumination, Nano Lett. **20**, 2602 (2020).

[31] S. B. Wang and C. T. Chan, Lateral optical force on chiral particles near a surface, Nat. Commun. **5**, 3307 (2014).

[32] Y. Liu, S. Hou, W. Zhang, and X. Zhang, Tunable manipulation of enantiomers by vector exceptional points, J. Phys. Chem. C **126**, 3127 (2022).

[33] K. Safkat, M. Rahim, and M. R. C. Mahdy, Optical sorting of a plasmonic or dielectric or chiral Mie object using a single metasurface, Ann. Phys. **534**, 2100402 (2021).

[34] Y. Xiang, X. Tang, Y. Fu, F. Lu, Y. Kuai, C. Min, J. Chen, P. Wang, J. R. Lakowicz, X. Yuan, and D. Zhang, Trapping metallic particles using focused Bloch surface waves, Nanoscale **12**, 1688 (2020).

[35] L. Gong, B. Gu, G. Rui, Y. Cui, Z. Zhu, and Q. Zhan, Optical forces of focused femtosecond laser pulses on nonlinear optical Rayleigh particles, Photonics Res. **6**, 138 (2018).

[36] Y. Roichman and D. G. Grier, Holographic assembly of quasicrystalline photonic heterostructures, Opt. Express **13**, 5434 (2005).

[37] C. F. Kuo and S. C. Chu, Dynamic control of the interference pattern of surface plasmon polaritons and its application to particle manipulation, Opt. Express **26**, 19123 (2018).

[38] T. Jaffe, N. Felgen, L. Gal, L. Kornblum, J. P. Reithmaier, C. Popov, and M. Orenstein, Deterministic arrays of epitaxially grown diamond nanopyramids, with embedded silicon-vacancy centers, Adv. Opt. Mater. **7**, 1800715 (2019).

[39] N. Rivera and I. Kaminer, Light–matter interactions with photonic quasiparticles, Nat. Rev. Phys. **2**, 538 (2020).

[40] X. G. Wang, L. Chotorlishvili, N. Arnold, V. K. Dugaev, I. Maznichenko, J. Barnas, P. A. Buczek, S. S. P. Parkin, and A. Ernst, Plasmonic Skyrmion Lattice Based on the Magnetoelectric Effect, Phys. Rev. Lett. **125**, 227201 (2020).

[41] W. Cai, O. Reinhardt, I. Kaminer, and F. J. G. de Abajo, Efficient orbital angular momentum transfer between plasmons and free electrons, Phys. Rev. B **98**, 045424 (2018).